



# Interstation $P_g$ and $S_g$ differential traveltime tomography in the northeastern margin of the Tibetan plateau: Implications for spatial extent of crustal flow and segmentation of the Longmenshan fault zone



Zhiwei Li<sup>a,\*</sup>, Sidao Ni<sup>a</sup>, Steven Roecker<sup>b</sup>

<sup>a</sup>State Key Laboratory of Geodesy and Earth's Dynamics, Institute of Geodesy and Geophysics, Chinese Academy of Sciences, Wuhan 430077, China

<sup>b</sup>Department of Earth and Environmental Sciences, Rensselaer Polytechnic Institute, Troy, NY 12180, USA

## ARTICLE INFO

### Article history:

Received 23 September 2013

Received in revised form 14 November 2013

Accepted 14 November 2013

Available online 14 December 2013

Edited by Vernon F. Cormier

### Keywords:

Northeastern Tibetan plateau

Crustal flow

Longmenshan fault zone

Minshan uplift

Traveltime difference tomography

$P_g$  and  $S_g$

## ABSTRACT

Interstation  $P_g$  and  $S_g$  differential traveltime tomography is performed in the northeastern margin of the Tibetan plateau, providing reliable mid-lower crustal velocity images while minimizing errors from earthquake mislocation and origin time. Prominent low  $P$  and  $S$  velocities ( $<5.9$  km/s for  $V_P$  and  $<3.5$  km/s for  $V_S$ ) in the northeastern Tibetan plateau are bound to the east by the Minjiang fault and the southwest segment of the Longmenshan fault zone (LMSFZ). In contrast, relatively high  $P$  and  $S$  velocities ( $>6.1$  km/s for  $V_P$  and  $>3.7$  km/s for  $V_S$ ) are found beneath the Sichuan basin and in the triangular region bound to the west by the Minjiang fault and to the east of the northeast segment of the LMSFZ. Significant low velocity anomalies suggest a weak mid-lower crust that flows beneath the eastern Tibetan plateau, while the high velocities beneath the Sichuan basin indicate a rigid, cold and stable crust. The strong lithospheric mantle beneath the Sichuan basin inferred from previous studies may act as a barrier to the eastward escape of crustal flow from the eastern Tibetan plateau. The segmentation of the LMSFZ is reconfirmed by the distinct mid-lower crustal velocities in the southwest and northeast segments. High velocity and low conductivity anomalies in the mid-lower crust beneath the eastern Minshan uplift and the western Qinling orogen suggest that no crustal flow reaches this area.

© 2013 Elsevier B.V. All rights reserved.

## 1. Introduction

The Tibetan plateau is the most intensive and extensive orogen on the Earth, and is characterized by the highest average elevations ( $>4000$  m) and almost double thickness crust ( $\sim 60$  km) within an area of around 2.5 million square kilometers (Fig. 1). The Indian-Eurasian continental collision has caused  $\sim 2000$  km shortening and the rapid uplift of the Tibetan plateau over the last 50 million years (Molnar and Tapponnier, 1975; Molnar, 1988). There are two models for the mechanism of the crustal thickening and plateau uplift: the plateau growth-backstop model (Tapponnier et al., 2001) and the crustal flow model (Royden et al., 1997; Clark and Royden, 2000). To the north of the Indian plate, crustal shortening could be responsible for the crustal thickening and plateau uplift. In contrast, in the eastern Tibetan plateau, the crustal flow model could better explain the crustal thickening. In this area, the crust has been thickened without significant upper crustal shortening along trust faults, suggesting deformation of the ductile lower

crust flow (Clark and Royden, 2000). For instance, the Longmenshan fault zone (LMSFZ) separates the eastern Tibetan plateau to the west from the Sichuan basin to the east (Fig. 2). Along the LMSFZ, the crustal flow model suggests that the ductile mid-lower crust is obstructed by the rigid, stable lithosphere of the Sichuan basin, resulting in the steepest topography gradient in the world and the rapid change in crustal thickness (from  $\sim 40$  km in the Sichuan basin to  $>60$  km in the eastern Tibetan plateau), but with no substantial horizontal motion (Burchfiel et al., 2008; Zhang et al., 2009; Wang et al., 2010; Li et al., 2011a, 2012). The isostatic and dynamic responses to lower crustal thickening, rather than the horizontal shortening of the upper crust, could explain these observations (Clark and Royden, 2000; Kirby et al., 2000).

The eastward crustal flow from the central Tibetan plateau is expected to divert south-eastward and north-eastward around the rigid Sichuan basin (Royden et al., 1997, 2008; Clark and Royden, 2000) (Fig. 1). The diversion of south-eastward crustal flow around the Sichuan–Yunnan rhombic block is manifested by gradually varying topography (Clark and Royden, 2000) and is corroborated by magnetotelluric (MT) imaging (Bai et al., 2010). However, the distribution of the crustal flow to the northwest of

\* Corresponding author. Tel.: +86 2786780717.

E-mail address: [zwli@whigg.ac.cn](mailto:zwli@whigg.ac.cn) (Z. Li).

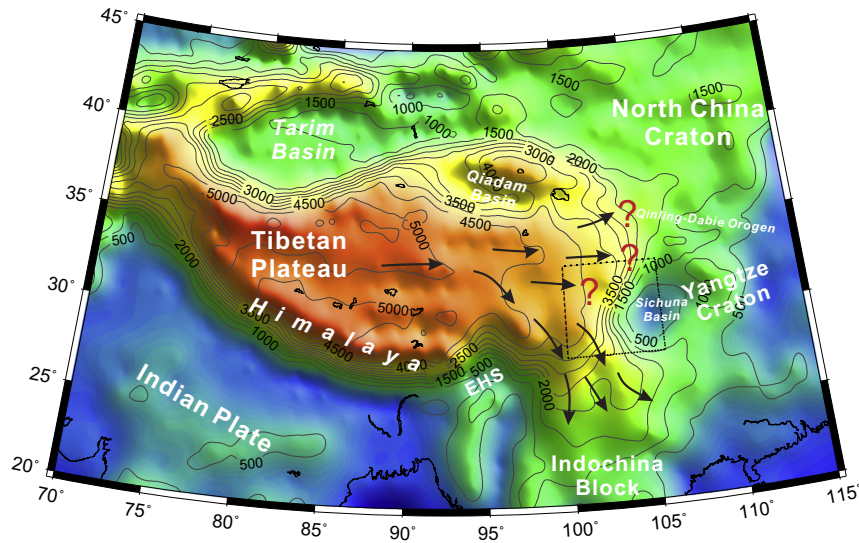


**Fig. 1.** Smoothed elevation of the Tibetan plateau and surrounding regions with contour intervals of 500 m. Possible lower crustal flow is labeled by black arrows after Clark and Royden (2000). Inset (dashed box) shows the study region in Fig. 2.

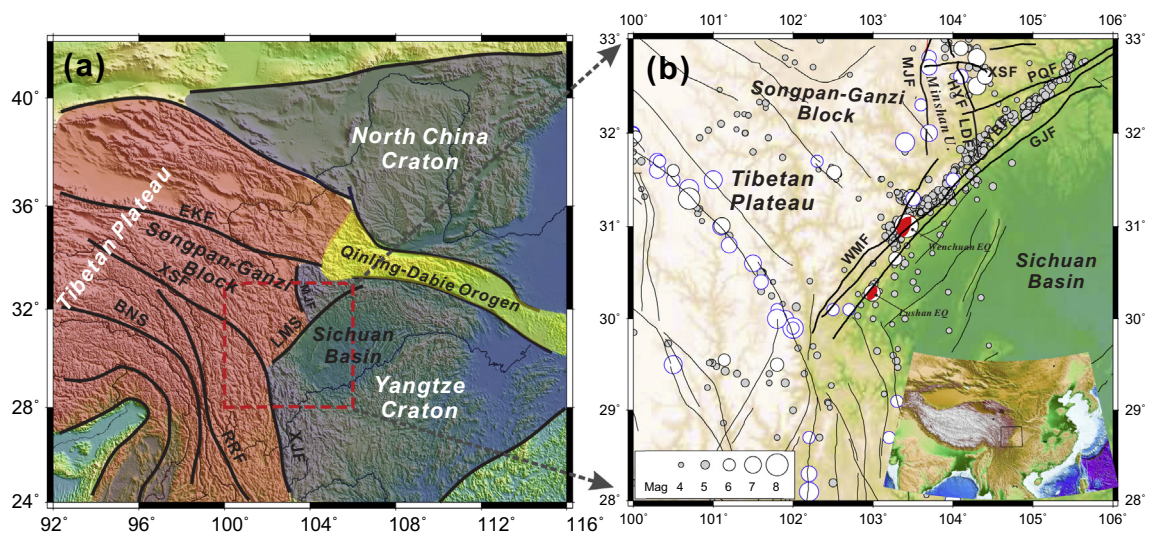


**Fig. 2.** (a) Regional tectonic map of the Tibetan plateau, Yangtze Craton and North China Craton. Major boundaries of blocks are shown with thick lines. The study region is indicated by a dashed box, which is located in the junction zone of the Tibetan plateau, Yangtze Craton and North China Craton, as well as the Qinling–Dabie Orogen. BNS, Bangong–Nujiang suture; EKF, east Kunlun fault; XSF, Xianshuihe fault; XJF, Xiaojiang fault; RRF, Red River fault; MJF, Minjiang fault. (b) Our study region showing topographic relief of the northeastern margin of the Tibetan plateau and Sichuan basin. Black lines indicate regional faults. M4 or greater earthquakes since the year of 1970 are plotted as black circles, and M6 or greater history earthquakes before the year of 1970 are plotted as blue circles (from the historical earthquake catalog provided by the China Earthquake Administration). The  $M_w$  7.9 Wenchuan earthquake on 12 May 2008 and the  $M_w$  6.6 Lushan earthquake on 20 April 2013 on the Longmenshan fault zone are also shown on this map (Li et al., 2013b). WMF, Wenchuan–Maoxian fault; GJF, Guanxian–Jiangyou fault; YBF, Yingxiu–Beichuan fault; MJF, Minjiang fault; HYF, Huya fault; LDF, Leidong fault; XSF, Xushan fault. (For interpretation of the references to colour in this figure legend, the reader is referred to the web version of this article.)

the Sichuan basin is unclear and requires more investigation. Two models have been proposed for the spatial extend of the north-eastern crustal flow. The first model features crustal flow obstructed by the Minshan uplift, and is supported by minor amounts of geodetically observed shortening and inferred tilting (Kirby et al., 2000). The second model suggests extended flow reaching the west Qinling–Dabie orogen to the north of the Sichuan basin (Fig. 2). The latter model is consistent with the topography variations to the east of the Minshan uplift and the rapid late Cenozoic cooling revealed from apatite fission-track thermochronology (Enkelmann et al., 2006). To validate either model, more evidence from the deeper crust is needed to resolve the spatial distribution of seismic velocities and electrical conductivity, in that the crustal

flow probably has low seismic velocity and high electrical conductivity (Royden et al., 2008; Bai et al., 2010).

A Cenozoic to Quaternary age uplift zone, the Minshan uplift is located near the junction of several tectonic blocks including the Tibetan plateau, the North China craton, the Yangtze craton and the Qinling–Dabie orogen (Chen et al., 1994) (Fig. 2). The Minshan uplift is elevated  $\sim 2000$  m above the mean value ( $\sim 3500$  m) of the adjacent plateau. The Minjing fault and the Huya fault border the Minshan uplift to the west and east, respectively. In 1976, three strong earthquakes (the Songpan earthquakes with magnitude of 7.2, 6.7 and 7.2) showed dominant thrust mechanisms on the Huya fault (Jones et al., 1984; Chen et al., 1994). The crustal flow model may explain the substantial thrust displacement of the three

earthquakes in a region of minor geodetically observed horizontal shortening. Using cooling rate estimates and stratigraphic studies, Kirby et al. (2000) speculated that the tilting and concomitant differential rock uplift in the Minshan mountain is related to the thickening of a weak, ductile mid-lower crust, which suggests crustal flow from the central Tibetan plateau.

Clues for spatial extent of crustal flow might also be found from segmentation of the LMSFZ, upon which the great 2008 Wenchuan earthquake occurred. The LMSFZ consists of a southwest segment and a northeast segment (Chen et al., 2007; Shen et al., 2009; Li et al., 2012). Significant differences are observed in the topography gradient (Clark and Royden, 2000), crustal and uppermost mantle velocity structure (Phillips et al., 2007; Lei and Zhao, 2009; Li et al., 2009a, 2010, 2011a, 2012; Liu et al., 2009; Wu et al., 2009; Xu et al., 2010; Yang et al., 2010), seismic activity, and rupture process and aftershock mechanisms of Wenchuan earthquake (Huang et al., 2008; Wang et al., 2008; Chen et al., 2009; Shen et al., 2009; Zheng et al., 2009, 2010, 2013; Luo et al., 2010) in the two segments. Tectonic evolution of the two segments also shows distinct characteristics (Chen et al., 2007; Jia et al., 2010b). Features such as a steep topography gradient and dominant thrust mechanism of rupture are well explained with crustal flow terminating at the southwest segment of the LMSFZ. The very different behavior of the northeast segment may imply absence of crustal flow in the northeasternmost part of the Tibetan plateau.

As the seismic network in the study region is sparse, velocity anomalies in the crust are difficult to image correctly in any great detail using 3-D traveltimes tomography. In such situations, 2-D tomography, adopting an approach similar to *Pn* tomography, can provide a robust view of different tectonic blocks (Hearn, 1984; Hearn et al., 2004; Steck et al., 2009, 2011). In this study, we conduct a 2-D traveltimes tomography to resolve the crustal velocity structure with interstation *Pg* and *Sg* traveltimes differences. Compared to absolute traveltimes tomography, differential traveltimes tomography has the advantage of minimizing errors from earthquake mislocation and origin time, thus leading more accurate estimates of  $V_p$  and  $V_s$  (Phillips et al., 2005; Seward et al., 2009; Li et al., 2011b, 2012), especially in regions where network coverage is sparse. In this paper we use interstation *Pg* and *Sg* traveltimes difference tomography to determine the mid- to lower crustal *P* and *S* velocity structure, from which we infer the spatial extent of crustal flow in and around the Minshan uplift, and the segmentation of the LMSFZ.

## 2. Method and data

### 2.1. Interstation *Pg* and *Sg* traveltimes difference tomography

The direct crustal phases *Pg* and *Sg* arrive at distances before the critically refracted *Pn* becomes the first arrival, and have been widely used for imaging the velocity structure of the crust (Zhang and Thurber, 2003; Jia et al., 2010a; Steck et al., 2009, 2011; Li et al., 2009b, 2013a,b). Although the *Pg* and *Sg* become secondary phases beyond the crossover distance, the signal-to-noise ratio (SNR) of the large amplitude *Pg* and *Sg* phases makes them easy to identify. Hence the arrivals of both first and the secondary *Pg* and *Sg* are abundant in the traveltimes dataset and can be very useful for crustal velocity imaging. Steck et al. (2009, 2011) proposed a tomography scheme to invert *Pg* and *Sg* traveltimes, which they used to obtain reliable crustal velocity images in the Eurasia continent and the western United States. The velocity structure, station terms and event terms are determined simultaneously assuming a great circle path between source and receiver, analogous to the approach used in *Pn* traveltimes tomography (Hearn, 1984; Hearn et al., 2004). The consistency of the velocity structures from *Pg* or

*Sg* 2-D tomography with 3-D traveltimes tomography and surface wave tomography in related studies demonstrates the effectiveness of this method (Steck et al., 2009, 2011).

The sparse distribution of seismic stations and the strongly heterogeneous crustal structure in both the eastern Tibetan plateau and the Sichuan basin can lead to large uncertainties in earthquake locations, particularly the focal depths. The absolute *Pg* and *Sg* traveltimes are contaminated by errors in the earthquake source parameters, which then compromises the tomographic result. Hence, it is beneficial to find a robust method to minimize these uncertainties in tomographic inversions of crustal structure. The advantages of traveltimes differences of seismic arrivals in better constraining earthquake relocations (Waldhauser and Ellsworth, 2000) and traveltimes tomography (Zhang and Thurber, 2003; Lin et al., 2010) are well documented. *Pn* traveltimes tomography is similarly improved by traveltimes difference data from an event recorded by two stations on approximately the same great circle path (Phillips et al., 2005; Seward et al., 2009; Li et al., 2011b, 2012). In this study, we modify the tomography scheme proposed by Steck et al. (2009, 2011) by using interstation *Pg* and *Sg* traveltimes differences rather than absolute traveltimes. Traveltimes difference from one earthquake to two stations effectively minimizes the errors from earthquake hypocenter and the origin time. The influence of crustal structure near the source region can also be reduced because the ray paths in the source-side (i.e., near the earthquake) crust are almost identical (Li et al., 2011b, 2012). The station term remains in the linear equations to correct the complex velocity structure near the station (e.g., low velocity sediment beneath the station). A damped LSQR method is utilized to solve the sparse linear equations (Paige and Saunders, 1982). In order to mitigate the introduction of artifacts appearing at only 1–2 grid points, a smoothing constraint is applied by a Laplacian operator when solving the linear equations.

### 2.2. Data

The dataset used in the inversion consists of *Pg* and *Sg* arrivals recorded by the China Earthquake Networks Center for earthquakes from January, 2000 to September, 2011. Only the phases labeled as *Pg* and *Sg* in the traveltimes catalog are extracted for additional data selection. Several criteria are imposed to control the quality of the initial dataset. We choose earthquakes with focal depth less than 30 km, at least 4 arrivals, and absolute residuals less than 3.0 s for the *Pg* and 4.0 s for the *Sg* arrival. Only those arrivals with epicenter distances greater than 120 km are selected to reduce model errors associated with small epicenter distances. For the initial dataset, we selected 211454 *Pg* arrivals from 12711 earthquakes at 280 stations, and 137640 *Sg* arrivals from 9953 earthquakes at 275 stations (Fig. 3). Interstation *Pg* and *Sg* traveltimes difference data are then chosen from the culled *Pg* and *Sg* arrivals with the following criteria: (1) the angle between the back azimuths at both stations is less than 4°, which helps satisfy the common great circle path requirement of the traveltimes difference tomography technique (Phillips et al., 2005; Li et al., 2012); (2) the distance between two stations for interstation traveltimes difference is greater than 10 km; and (3) the traveltimes difference residuals are less than 3.0 s for *Pg* arrivals, and 4.0 s for *Sg* arrivals. We also require that traveltimes difference residuals are less than 20% of the traveltimes difference itself. After these preprocessing steps, a set of 5427 *Pg* traveltimes difference pairs from 3226 earthquakes, and 4511 *Sg* traveltimes difference pairs from 2968 earthquakes remain for the tomographic inversion. The focal depths of many of the earthquakes used for *Pg* and *Sg* traveltimes difference are greater than 10 km (Fig. 4), thus ensuring that seismic rays sample the mid to lower crust. The data coverage is

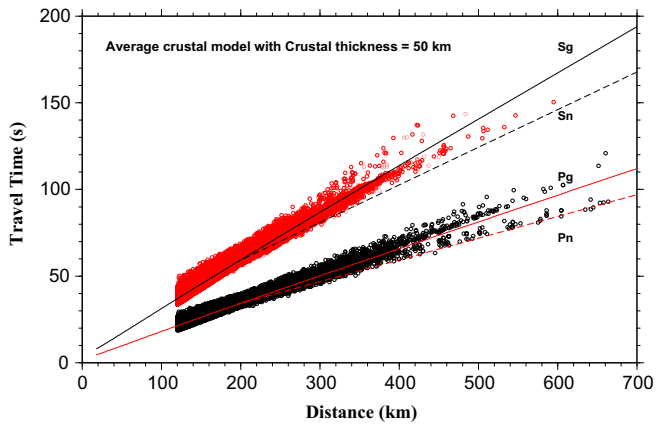


**Fig. 3.**  $P_g$  and  $S_g$  traveltimes after initial data selection. Synthetic traveltimes of  $P_g$ ,  $P_n$ ,  $S_g$  and  $S_n$  waves are plotted with the observed traveltimes. 1-D  $P$  and  $S$  velocity models with a 50 km Moho depth and a source at 10 km depth are used to calculate synthetic traveltimes of  $P_g$ ,  $P_n$ ,  $S_g$  and  $S_n$  waves (Xu et al., 2010; Li et al., 2011a).

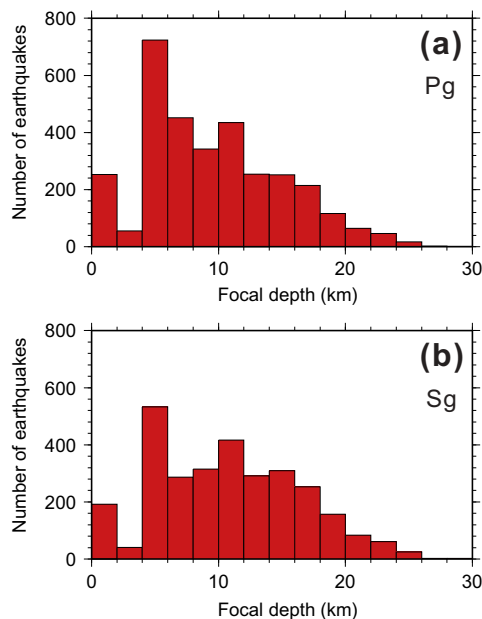


**Fig. 4.** Focal depth distribution of earthquakes used in this study for  $P_g$  (a) and  $S_g$  (b) traveltime difference data.

reasonably good in the northeastern margin of the Tibetan plateau and the Sichuan basin near the LMSFZ (Fig. 5).

### 3. Results

#### 3.1. Initial model

The initial apparent  $P_g$  and  $S_g$  velocities are determined by linear fitting with interstation traveltime difference data, which are  $\sim 6.0$  km/s for  $P_g$  and  $\sim 3.6$  km/s for  $S_g$  (Fig. 6). These velocities are close to the average velocities in the mid-lower crust determined by deep seismic sounding (Li et al., 2006), receiver functions (Liu et al., 2009; Wang et al., 2010), ambient noise surface wave tomography (Li et al., 2009a, 2010) and local earthquake tomography (Pei et al., 2010; Xu et al., 2010; Li et al., 2011a, 2012) in this area. The linear trend is quite clear in a plot of  $P_g$  and  $S_g$  traveltime

difference versus interstation distance (Fig. 6a and c), the slope of which is equal to the average  $P_g$  or  $S_g$  velocity. Lateral variations in velocity are more easily recognized in plots of traveltime differences with reduced velocity (6.0 km/s for  $P_g$ , and 3.6 km/s for  $S_g$ ) versus epicenter distance difference for  $P_g$  and  $S_g$  arrivals (Fig. 5b and d).

#### 3.2. Results

As a result of the inversion, the root-mean-square (RMS) of residuals is reduced from 0.92 s for the starting model to 0.47 s for  $P_g$  traveltime differences (a 49% reduction in residuals) (Fig. 7a and b), and from 1.25 s for the starting model to 0.62 s for  $S_g$  traveltime differences (a 50% reduction in residuals) (Fig. 7c and d). We conducted trial tomographic inversions for different grid-spacings of  $1.0^\circ \times 1.0^\circ$ ,  $0.5^\circ \times 0.5^\circ$  and  $0.25^\circ \times 0.25^\circ$  in longitudinal and latitudinal directions. The preferred models fit the observed data well despite their different grid spacing, and also show similar patterns of velocity variations in the study region, demonstrating the robustness of the tomographic inversion. In order to avoid anomalies in the tomographic images that are below the resolution limit while retaining reliable details, a model with grid-spacing of  $0.5^\circ \times 0.5^\circ$  was chosen for analyzing the crustal structure. In the discussion that follows, only the prominent, stable velocity anomalies are reviewed.

A series of checkerboard tests with different anomaly sizes ( $0.5^\circ \times 0.5^\circ$  and  $1.0^\circ \times 1.0^\circ$ ) are performed with  $0.5^\circ \times 0.5^\circ$  grid-spacing to estimate the resolution of the tomography models (Fig. 8). Gaussian noise (0.2 s for  $P_g$  and 0.3 s for  $S_g$ ) is added to the synthetic traveltimes to simulate picking errors. The recovered checkerboards suggest that for most areas with good ray path coverage, the velocity anomalies with different sizes can be well resolved, especially in the eastern Tibetan plateau, the Sichuan basin and the Minshan uplift in the vicinity of the LMSFZ. Due to the absence of crossing ray paths, the velocity patterns near the edges of the study region are poorly resolved.

For clarity, the final models for  $P$  (Fig. 9a) and  $S$  (Fig. 9b) velocities are superimposed upon shaded topography. The most prominent features in these models are the low  $P$  and  $S$  velocity anomalies in the northeastern margin of the Tibetan plateau and the prominent high  $P$  and  $S$  velocity anomalies in the Sichuan basin. Prominent low  $P$  and  $S$  velocities ( $< 5.9$  km/s for  $V_p$  and  $< 3.5$  km/s for  $V_s$ ) are bounded by the southwest segment of the LMSFZ and the Minjiang Uplift are imaged beneath the eastern Tibetan plateau and the Sichuan-Yunnan rhombic block. High  $P$  and  $S$  velocities ( $> 6.1$  km/s for  $V_p$  and  $> 3.7$  km/s for  $V_s$ ) are found beneath the Sichuan basin. The southwest segment of the LMSFZ is parallel to the boundary separating the low and high  $P$  and  $S$  velocities, whereas moderately high  $P$  and  $S$  velocities ( $> 6.0$  km/s for  $V_p$  and  $> 3.6$  km/s for  $V_s$ ) are also found in the northeastern tip of the Tibetan plateau defined by the northeastern segment of the LMSFZ and the Minshan uplift.

#### 4. Discussion

The determination of the depth range sampled by the  $P_g$  and  $S_g$  differential traveltime tomography, as in  $P_g$  or  $S_g$  absolute traveltime tomography, is not trivial. While there are several models of  $P_g$  (or  $S_g$ ) propagation in the crust (e.g., one trapped in the upper crust, the other reverberations in the whole crust), previous studies agree that the  $P_g$  (or  $S_g$ ) 2-D tomography represents crustal structure for some average depth range (Steck et al., 2009, 2011). As a means of interpretation, Steck et al. (2009, 2011) suggest that the dominant mode of propagation and the depth extent of the tomography images can be qualitatively estimated by analyzing the data

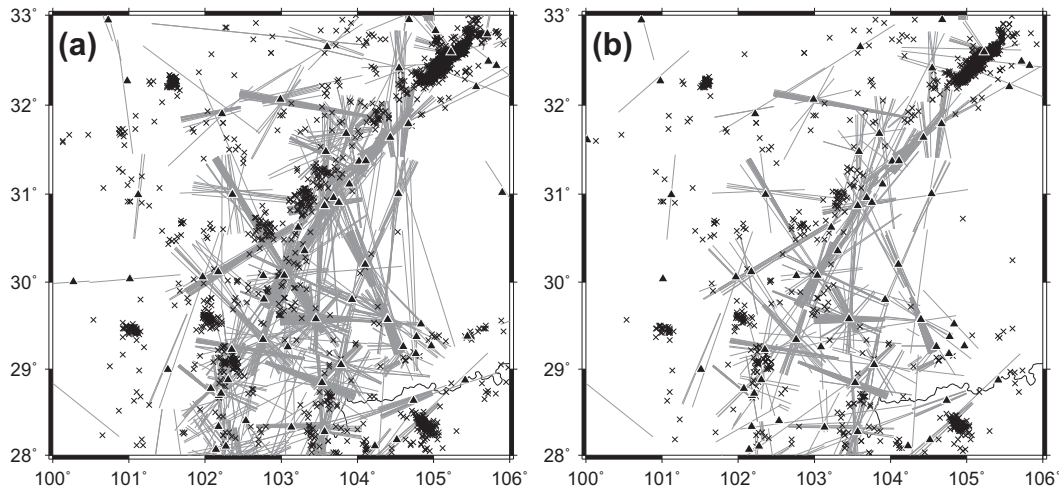


**Fig. 5.** (a)  $P_g$  and (b)  $S_g$  traveltime difference data from stations (triangles) and earthquake (crosses) used in the tomographic inversion. Gray lines indicate the ray paths approximately sampling the middle crust. Good ray path coverage is evident in the Longmenshan fault zone and adjacent regions.

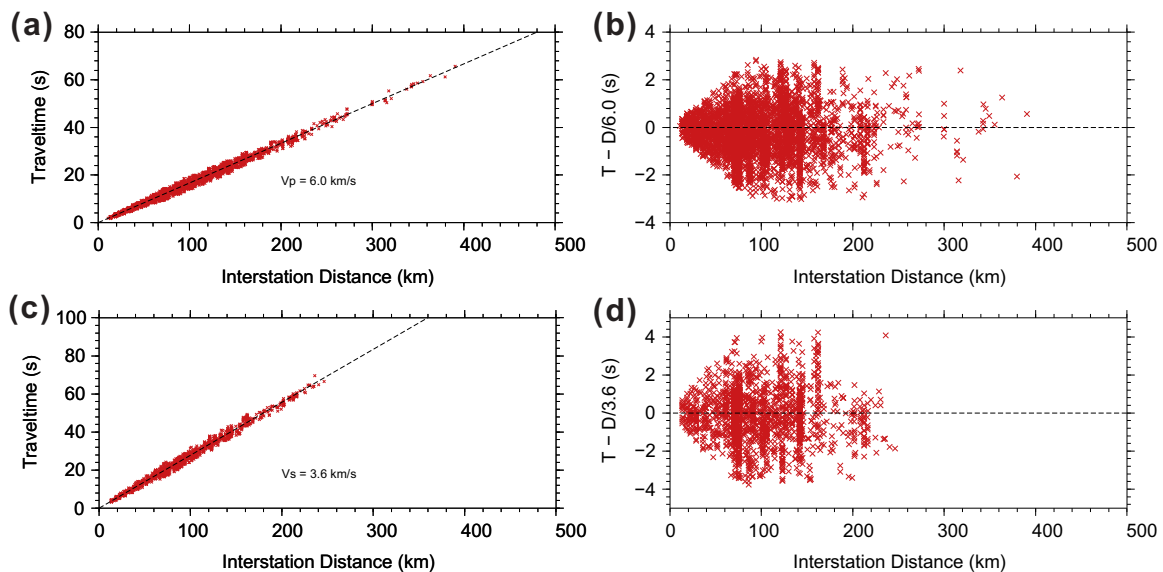


**Fig. 6.** (a) Average  $P$  velocity of 6.0 km/s in the middle crust as determined by regression of interstation  $P_g$  traveltime differences (represented by the dashed line) versus interstation distances.  $P_g$  differential traveltimes with interstation distance less than 10 km are excluded from the inversion. (b) Reduced traveltime differences with an average  $P$  velocity of 6.0 km/s. (c) Same figure as Fig. 3a but for average  $S$  velocity of 3.6 km/s. (d) Same figure as Fig. 3b but for reduced traveltime differences with an average  $S$  velocity of 3.6 km/s.

used in the inversion and by comparing results to previous studies. The  $P_g$  and  $S_g$  traveltimes used in the inversion are all recorded with epicentral distances greater than 120 km (Fig. 3), and most interstation distances are greater than 100 km (Fig. 6a and d). The focal depths of many earthquakes are also greater than 10 km (Fig. 4), which could make ray path sampling mainly in the middle crust. Moreover, for earthquakes with focal depths greater than 15 km and interstation distance greater than 300 km (the epicenter distance will be greater), the sampling region could be as deep as the base of the middle crust and top of the lower crust. We also compared our tomographic images with velocity structures determined from 3-D  $P$  and  $S$  traveltime tomography (Lei and Zhao, 2009; Wu et al., 2009; Xu et al., 2010; Li et al., 2011a), ambient noise surface wave tomography (Li et al., 2009a, 2010; Yang et al., 2010; Zheng et al., 2013), receiver function inversions (Liu et al., 2009; Zhang et al., 2009) and deep seismic sounding (Jia et al., 2010a). The overall consistency from these

comparisons shows that the velocity anomalies are similar for the crustal structures between 20 and 40 km depth in the northeastern Tibetan plateau, and somewhat shallower in the thinner crust of the Sichuan basin. Therefore, the tomographic images obtained in this study probably reflect the velocity variations of the middle crust and the top of lower crust on average. The prominent features of low velocities beneath the northeastern Tibetan plateau and the high velocities beneath the Sichuan basin are similar to those from previous studies with seismic data (Fig. 9). Although the amplitudes of the velocity anomalies from these studies are somewhat different from each other, the patterns remain largely similar. Multidisciplinary data also provide independent information in this region. MT profiles cross the LMSFZ reveal high and low conductivity material in the mid-lower crust beneath the eastern Tibetan plateau and the the Sichuan basin, respectively (Wang et al., 2009; Zhao et al., 2009; Bai et al., 2010). A density inversion with Bouguer gravity also indicates low densities in both the mid-

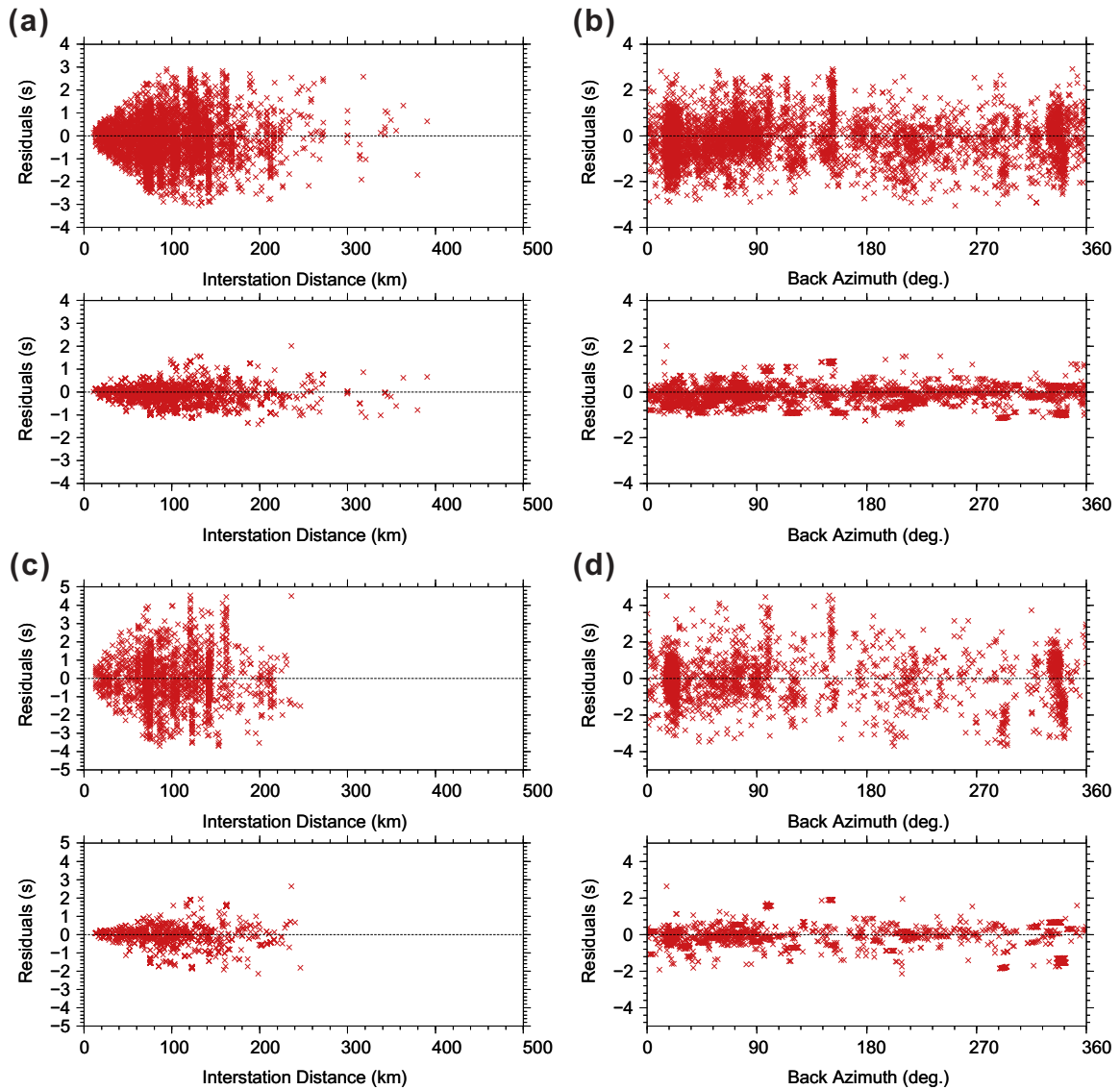


**Fig. 7.** (a) Comparison of  $P_g$  traveltime difference residuals before (upper row) and after (lower row) the tomographic inversion, plotted against interstation distances. (b) Same figure as Fig. 5a but for variation of  $P_g$  traveltime difference residuals plotted against back azimuth. (c) Same figure as Fig. 5a but for  $S_g$  traveltime difference residuals. (d) Same figure as Fig. 5b but for  $S_g$  traveltime difference residuals.

upper crust and the lower crust (Lou et al., 2008). The geophysical anomalies found in the above studies are consistent with the velocity anomalies in our results, demonstrating the robustness of this anomaly pattern. Although one might want to show a  $V_P/V_S$  image obtained from the direct division of the  $V_P$  model by the  $V_S$  model, possible discrepancies in the sampling depths of  $P_g$  and  $S_g$  data, as well as the amplified errors resulting from direct division, prevent us from attempting this here.

#### 4.1. Implication for crustal flow in the eastern Tibetan plateau

In the eastern Tibetan plateau, crustal thickening and uplift are believed to be mostly due to deformation within the ductile lower crust, as suggested by the absence of significant upper crustal shortening along the thrust faults (Burchfiel et al., 1995; Clark and Royden, 2000). The low  $P$  and  $S$  velocities (about 5–6% lower than the average for both  $P$  and  $S$  velocities) beneath the eastern Tibetan plateau suggest a weak, ductile mid-lower crust. In contrast, high  $P$  and  $S$  velocities (about 4–5% higher than the average for both  $P$  and  $S$  velocities) beneath the Sichuan basin imply a

strong, rigid mid-lower crust. Similar characteristics of the mantle lid are revealed as well by  $P_n$  tomography with regular and traveltime difference tomography (Hearn et al., 2004; Phillips et al., 2005; Li et al., 2012). Since the  $P_n$  velocity is sensitive to temperature, fluid content and pressure (McNamara et al., 1997; Hearn et al., 2004), one possible interpretation for the low  $P_n$  velocity anomaly in the eastern Tibetan plateau is the increase in temperature caused by hot asthenosphere beneath a very thin lithosphere (70–80 km) (Zhang et al., 2009, 2010) as evidenced by low velocity anomalies (1–3% lower than the background) at 90–150 km depth (Guo et al., 2009). A hot mantle lid could increase the temperature of the mid-lower crust by heat conduction. Based on MT profiles in the eastern Tibetan plateau, Bai et al. (2010) proposed that the high conductivity of the mid-lower crust (at a depth of 20–40 km) could be attributed to an elevated aqueous fluid content (5–20%). For a double-thickened, generic granitoid continental crust, the existence of aqueous fluid in a global average mantle heat flux will lower the partial melting temperature ( $\sim 600^\circ\text{C}$ ) (Nelson et al., 1996). In addition, the increased temperature of the mantle lid could also promote partial melting in the mid-lower crust. Partial

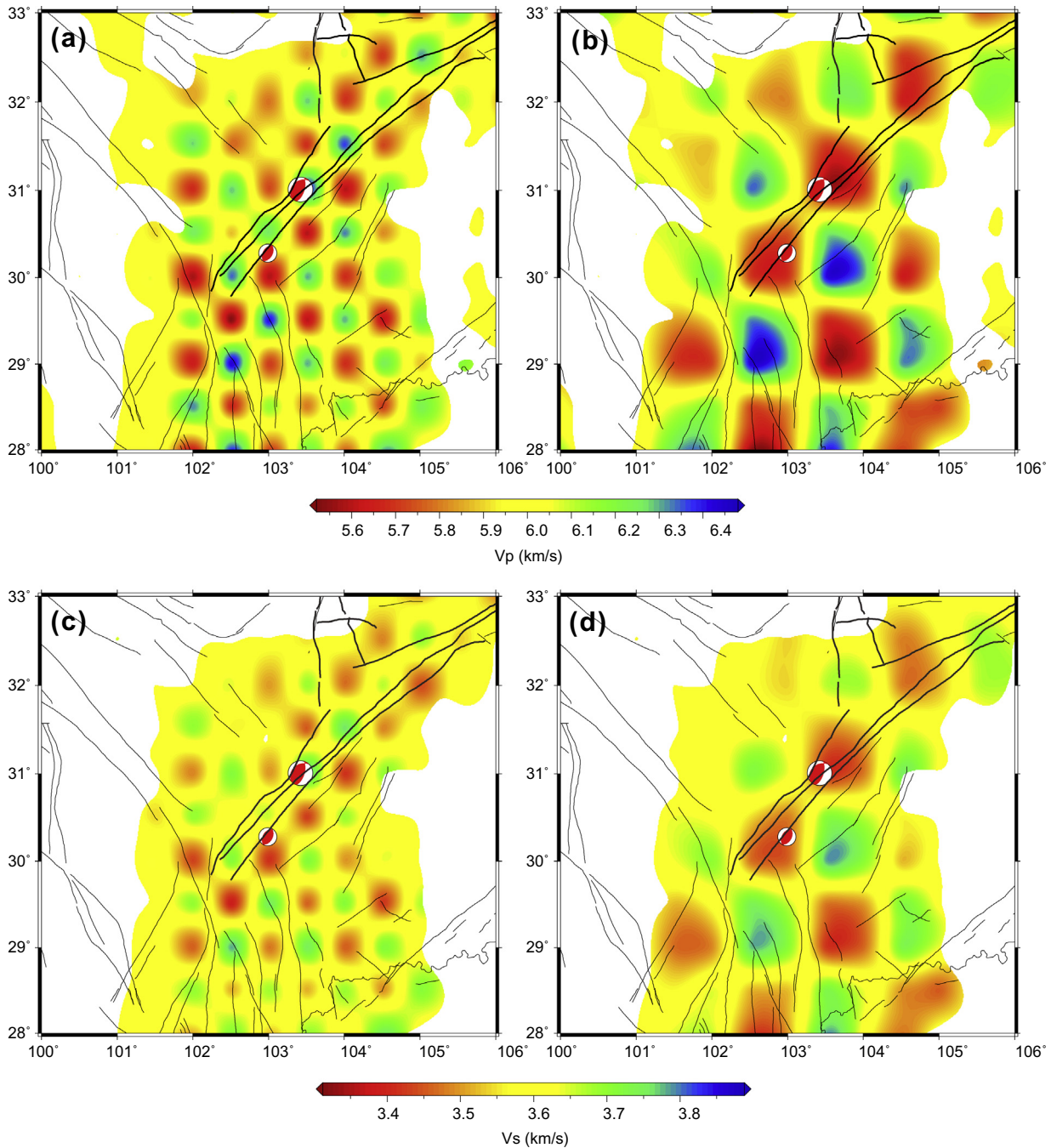


**Fig. 8.** Checkerboard resolution tests for different anomaly sizes. (a) and (b) are for  $P$  velocity models with inversion node spacing of  $0.5^\circ \times 0.5^\circ$  and  $1.0^\circ \times 1.0^\circ$ , respectively. (c) and (d) are for  $S$  velocity models with inversion node spacing of  $0.5^\circ \times 0.5^\circ$  and  $1.0^\circ \times 1.0^\circ$ , respectively. Only the velocities with ray path hit counts greater than 2 are shown.

melting of  $\sim 5\%$  or increased fluid content could decrease the viscosity of the crust materials by an order of magnitude, which can make mid-lower crustal flow possible (Rosenberg and Handy, 2005; Beaumont et al., 2001). A combination of aqueous fluids and/or partial melt could provide a possible explanation for the high conductivity and low  $S$  velocity in the mid-lower crust. Li et al. (2003) proposed that a thin layer of aqueous fluids (100–200 m in thickness) overlying a partial melting zone ( $>10$  km in thickness) is the most probable interpretation for the high conductivity and low  $S$  velocity of the middle crust in southern Tibet. In the eastern Tibetan plateau, low velocities found in the mantle lid and upper mantle at depths 90–150 km may indicate hot man-

tle. The temperature of the mid-lower crust could be substantially elevated, with subsequent partial melting, may, in combination with possible aqueous fluids, be a viable explanation for the prominent low  $P$  and  $S$  velocities shown in this study. It is difficult to quantify the interconnectivity of the mid-lower crustal materials, and it is nontrivial to determine the proportions of partial melting and aqueous fluids. Nevertheless, in order to generate crustal flow, at least 5% partial melting or fluid content are required to sufficiently reduce the strength and lower the viscosity of the mid-lower crust (Rosenberg and Handy, 2005; Beaumont et al., 2001).

In contrast to the low velocity anomalies in the northeastern Tibetan plateau to the west of Minshan, the Sichuan basin is charac-

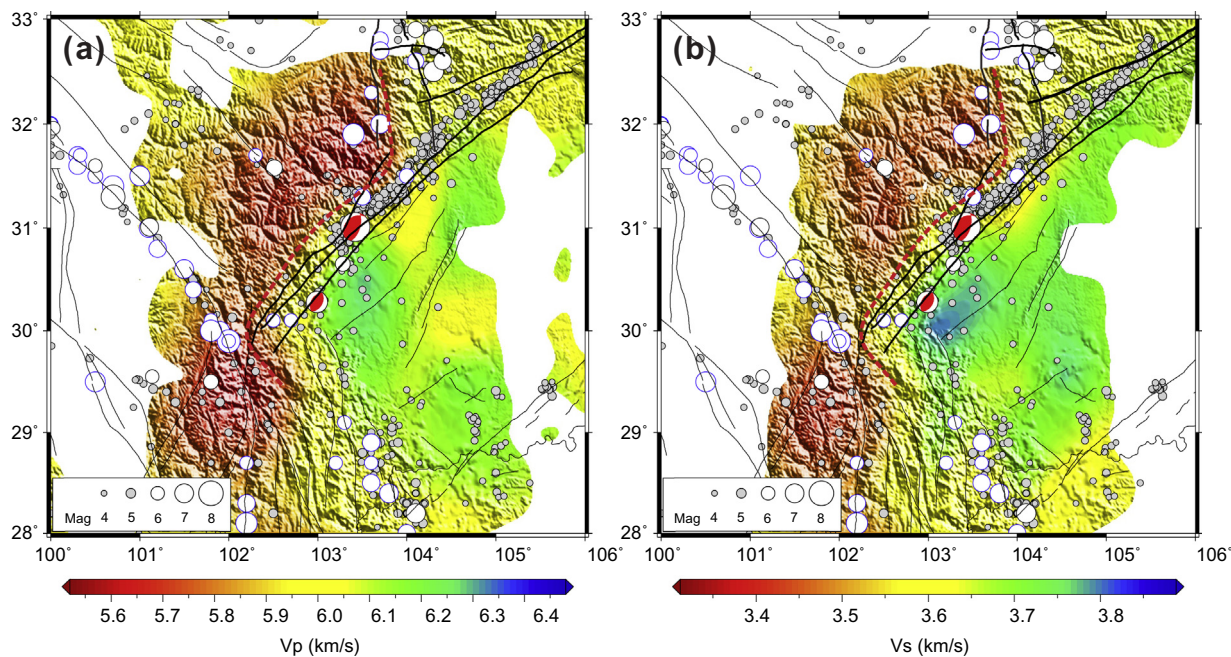


**Fig. 9.** (a)  $P_g$  and (b)  $S_g$  velocities from the tomographic inversion with interstation  $P_g$  and  $S_g$  traveltime time differences, respectively. Only the velocities with ray path hit counts greater than 2 are shown. Regional faults and history earthquakes (see Fig. 2b for details) are overlaid on the velocity images. The red dashed lines indicate the possible lower crustal flow according to low  $P$  and  $S$  velocity anomalies. (For interpretation of the references to colour in this figure legend, the reader is referred to the web version of this article.)

terized by prominent high  $P$  and  $S$  velocities. High  $P$  and  $S$  velocities in the crust (Lei and Zhao, 2009; Wu et al., 2009; Li et al., 2010, 2011a; Xu et al., 2010; Yang et al., 2010; Wei et al., 2013; Zheng et al., 2013), low electrical conductivity (Wang et al., 2009; Zhao et al., 2009; Bai et al., 2010; Zhan et al., 2013) and high  $P_n$  velocity in the uppermost mantle (Hearn et al., 2004; Phillips et al., 2005; Li et al., 2012) suggest a rigid, cold and strong mid-lower crust and lithospheric mantle beneath the Sichuan basin. A strong Sichuan basin may act as a barrier to the eastward escape crustal flow beneath the eastern Tibetan plateau. Steep, abrupt margins on topography are characterized along the southwest segment of the LMSFZ, while low-gradient margins are found along the northeast segment of the LMSFZ and in the southeast Tibetan plateau. The significant change in topography gradient suggests that the eastward crustal flow from the central Tibetan plateau diverts southward around the strong Sichuan basin (Royden et al., 1997, 2008; Clark and Royden, 2000; Zhang et al., 2010) (Fig. 1). The southward crustal flow in the Sichuan–Yunan rhombic block has been delineated by seismic and MT imaging (Yao et al., 2008; Bai et al., 2010). Our tomography results suggest that the crustal flow terminates at the Minshan uplift, and does not reach the western Qinling orogen.

#### 4.2. Implication for absence of crustal flow in the west Qinling orogen

The Minshan uplift is located in the tectonic junction between the Tibetan plateau, the North China craton, the Yangtze craton, and the Qinling–Dabie orogen (Fig. 2). The Minshan uplift is a Cenozoic to Quaternary age uplift and is elevated  $\sim 2000$  m above the mean value ( $\sim 3500$  m) of the adjacent plateau (Chen et al., 1994). Enkelmann et al. (2006) proposed that crustal flow has been diverted to the southwest Qinling orogen based on the cooling/exhumation history of Qinling orogen by apatite fission-track thermochronology. However, the  $P$  and  $S$  tomographic results in this study suggest that the Minshan uplift separates the significant low velocities to its west from the relatively high velocities to its east, with no low velocity anomalies beneath the Minshan uplift

(Fig. 9). The feature is also clear in the  $P$  wave velocity images at 25 and 40 km depth in this area from 3-D traveltime tomography (Wei et al., 2013). The north–south MT profile crossing the west Qinling orogen reveals a narrow ( $\sim 40$  km in width) high conductivity zone from the surface to  $\sim 30$  km depth, bounded by two prominent, broad (80–120 km in width) low conductivity anomalies on its north and south sides (Zhao et al., 2009). Zhao et al. (2009) proposed that the narrow high conductivity zone could be attributed to upwardly migrating fluids along the fault zone resulting from the collision between the Sichuan basin to the south and the Ordos block to the north, rather than the crustal flow from the eastern Tibetan plateau. The relative high velocities beneath the west Minshan uplift and the west Qinling orogen imply no apparent crustal flow from the eastern Tibetan plateau into this area.

Kirby et al. (2000) proposed that the tilting and concomitant differential rock uplift in the Minshan mountain may be attributed to the thickening and deformation of a weak, ductile mid-lower crust. However, as shown in our tomographic results, relatively low  $P$  and  $S$  velocities are limited at the west Minshan uplift near the Minjiang fault, rather than extended to the whole Minshan uplift (Fig. 9). According to the MT profile crossing the Sichuan Basin and the Songpan–Ganzi block (Wang et al., 2009), a high conductivity layer at 30–40 km depth beneath the Minshan uplift gradually vanishes from west to east. Based on geological surveys and tectonic analysis, the Songpan–Ganzi block overlies the South China basement consisting of a Paleozoic cratonic sequence beneath Triassic strata (Yin and Harrison, 2000). The Minshan uplift to the west of the Minjiang fault also belongs to the Yangtze craton (Li et al., 2007). The high conductivity layer at 30–40 km depth beneath the west Minshan uplift suggests the presence of Tethyan oceanic crustal materials remaining after the break-up of the Songpan–Ganzi block and Yangtze craton (Yin et al., 1999). Furthermore, as there is also no evidence for crustal flow beneath the west Qinling orogen, the high crustal velocities beneath the Minshan uplift suggest a relatively strong crust, implying that crustal flow does not extend to the eastern part of the Minshan uplift. Crustal flow near the Minshan fault could thicken and deform

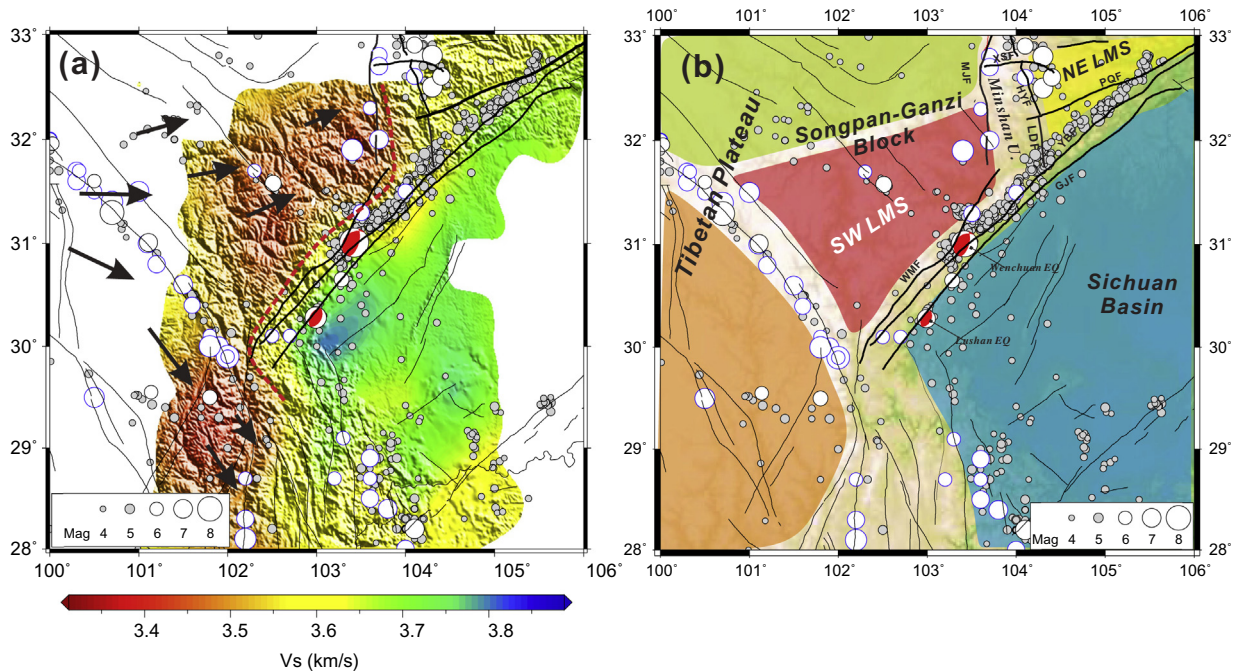


**Fig. 10.** (a) Interpreted tectonic units and possible mid-lower crustal flow in the northeastern margin of the Tibetan plateau and Longmenshan fault zone based on our results. The Longmenshan mountain can be divided into southwest (SW LMS) and northeast (NE LMS) segments by the Huya and Leidong faults (or the Minshan uplift). Weak lower crustal flow may exist beneath the southwest Longmenshan mountain based on the low  $P$  and  $S$  velocity anomalies in the mid-lower crust. In contrast, the northeast Longmenshan mountain in the west Qinlin–Dabie orogen shows normal mid-lower crustal velocity, suggesting relatively strong mid-lower crust in this area. Therefore, no evidence is found for weak lower crustal flow as proposed by Enkelmann et al. (2006). (b) Identification of tectonic blocks by Shen et al. (2009), which corroborate our results.

the weak, ductile mid-lower crust and be responsible for the uplift of the Minshan mountain. The 1976 Songpan earthquakes on the Huya fault could be a result of this crustal flow extrusion and deformation (Chen et al., 1994).

#### 4.3. Implication for the segmentation of the LMSFZ

The Huya and Leidong faults to the east of Minshan uplift correspond to anomalous gradients in gravity and topography that approximately separate the LMSFZ into southwest and the northeast segments (Fig. 10) (Chen et al., 2007). These gradients also change significantly along the LMSFZ at its southwest and northeast segments (Chen et al., 2007; Li et al., 2012). The southwest segment forms a sharp boundary separating the prominent low velocity in the eastern Tibetan plateau from the high velocity in the Sichuan basin (Fig. 9). In contrast, velocity contrasts are not strong across the northeast segment. Similar features are found for the  $S$  velocities in mid-lower crust from ambient noise surface wave tomography (Yang et al., 2010; Zheng et al., 2013) and the  $Pn$  velocity in the uppermost mantle (Li et al., 2012). Electrical conductivities derived from MT profiles across the southwest and northeast segments also show very distinct features. Beneath the southwest segment of the LMSFZ, electrical conductivity anomalies are steeply dipping and vary by about  $10^3$  (Bai et al., 2010; Zhan et al., 2013). In the northeast segment, the change in electrical conductivity is much gentler with contrasts on the order of  $10^2$  (Wang et al., 2009; Zhao et al., 2009). The fault geometry and slip distribution of the Wenchuan earthquake derived from geodetic data also show distinct characteristics on the two segments: on the southwest segment, the fault plane dips moderately to the northwest, while on the northeast segment, it becomes nearly vertical (Shen et al., 2009). The rupture process reveals two relatively independent ruptures on the two segments (Ji and Hayes, 2008; Wang et al., 2008). The southwest segment is dominated by thrust motion with a dip angle of 30–50°, while the northeast segment is

characterized by both thrust and strike-slip with a dip angle of 70–90° (Wang et al., 2008; Xu et al., 2008; Zhang et al., 2008; Zheng et al., 2009, 2010; Luo et al., 2010).

As stated above, the segmentation of the LMSFZ is reflected in the significant changes in seismic velocities in the mid-lower crust for the southwest and northeast segments of the LMSFZ, as are contrasts in  $Pn$  velocity, gradients in gravity and topography, seismic activity, rupture processes and historical seismicity. If the crustal flow stops at the Minshan uplift, then the segmentation of LMSFZ may result from the southwest segment being deformed by crustal flow while the northeast segment, being free from effects of crustal flow, may be driven only by regular crustal dynamics (e.g., faulted blocks, non-crustal flow). Thus, the segmentation of the LMSFZ supports the hypothesis that crustal flow has not reached the western Qinling orogen.

## 5. Conclusions

Interstation  $Pg$  and  $Sg$  differential traveltimes tomography is conducted in the northeastern margin of the Tibetan plateau. The tomographic results obtained in this study are consistent with those from previous studies. However, with advantages from the usage of interstation differential traveltimes, errors from earthquake mislocation and unknown origin time are minimized. The tomographic images in this study likely represent the average velocity variations of the middle crust and the top of lower crust, but the  $Pg$  and  $Sg$  velocities probably sample different depth ranges. Significantly low velocity anomalies beneath the northeastern Tibetan plateau in the mid-lower crust, and prominent high velocities beneath the Sichuan basin are confirmed by our results. These anomalies are consistent with proposed mid-lower crustal flow beneath the eastern Tibetan plateau and a rigid and stable crust beneath the Sichuan basin. The segmentation of the LMSFZ is also confirmed by the mid-lower crustal velocities in the southwest and northeast segments, as suggested also by contrasts in  $Pn$

velocity, gravity and topography gradients, seismic activity, rupture processes and historical seismicity obtained by previous studies. The eastward crustal flow from the central Tibetan plateau is expected to divert southward and northward around the rigid Sichuan basin. The relatively high velocity anomalies in the mid-lower crust beneath the east Minshan uplift and western Qinling orogen found in our study, and the low conductivity anomalies from MT profiles, show no clear crustal flow reaching this area. Relatively low velocities to the west of the Minshan uplift suggest that the mid-lower crust may be deformed by the lower crustal flow, which could be responsible for its uplift.

## Acknowledgements

We are grateful to the China Earthquake Network Center for providing the seismic arrival time data used in this study. We thank the Editor, Prof. Vernon Cormier and anonymous reviewers for their valuable comments. This work was supported by National Basic Research Program of China (grant Nos. 2013CB733204 and 2013CB733203), National Natural Science Foundation of China (grant Nos. 41304045 and 41210005) and special funds from State Key Laboratory of Geodesy and Earth's Dynamics.

## References

- Bai, D.H., Unsworth, M.J., Meju, M.A., et al., 2010. Crustal deformation of the eastern Tibetan plateau revealed by magnetotelluric imaging. *Nat. Geosci.* 3 (5), 358–362.
- Beaumont, C., Jamieson, R.A., Nguyen, M.H., Lee, B., 2001. Himalayan tectonics explained by extrusion of a low-viscosity crustal channel coupled to focused surface denudation. *Nature* 414, 738–742.
- Burchfiel, B.C., Chen, Z.L., Liu, Y.P., Royden, L.H., 1995. Tectonics of the Longmen Shan and adjacent regions, Central China. *Int. Geol. Rev.* 37, 661–735.
- Burchfiel, B.C., Royden, L.H., van der Hilst, R.D., et al., 2008. A geological and geophysical context for the Wenchuan earthquake of 12 May 2008, Sichuan, People's Republic of China. *GSA Today* 18, 4–11.
- Chen, S.F., Wilson, C., Deng, Q.D., Zhao, X.L., Luo, Z.L., 1994. Active faulting and block movement associated with large earthquakes in the Min Shan and Longmen Mountains, northeastern Tibetan plateau. *J. Geophys. Res.* 99 (B12), 24025–24038.
- Chen, G.G., Ji, F.J., Zhou, R.J., et al., 2007. Primary research of activity segmentation of Longmenshan fault zone since Late-Quaternary. *Seismol. Geol.* 29 (3), 657–673.
- Chen, J.H., Liu, Q.Y., Li, S.C., et al., 2009. Seismotectonic study by relocation of the Wenchuan  $M_s$  8.0 earthquake sequence (in Chinese). *Chin. J. Geophys.* 52 (2), 390–397.
- Clark, M.K., Royden, L.H., 2000. Topographic ooze: building the eastern margin of Tibet by lower crustal flow. *Geology* 28 (8), 703–706.
- Enkelmann, E., Ratschbacher, L., Jonckheere, R., Nestler, M., Gloaguen, R., Hacker, B.R., Zhang, Y.Q., Ma, Y.S., 2006. Cenozoic exhumation and deformation of northeastern Tibet and the Qinling: Is Tibetan lower crustal flow diverging around the Sichuan Basin. *Geol. Soc. Am. Bull.* 118 (5–6), 651–671.
- Guo, B., Liu, Q., Chen, J., et al., 2009. Telesismic  $P$ -wave tomography of the crust and upper mantle in Longmen Shan area, west Sichuan (in Chinese). *Chin. J. Geophys.* 52 (2), 346–355.
- Hearn, T.M., 1984.  $Pn$  Travel times in southern California. *J. Geophys. Res.* 89, 1843–1855.
- Hearn, T.M., Wang, S.Y., Ni, J.F., Xu, Z., Yu, Y., Zhang, X., 2004. Uppermost mantle velocities beneath China and surrounding regions. *J. Geophys. Res.* 109, B11301.
- Huang, Y., Wu, J.P., Zhang, T.Z., et al., 2008. Relocation of the  $M_s$  8.0 Wenchuan earthquake and its aftershock sequence. *Sci. China Ser. D-Earth Sci.* 51 (12), 1703–1711.
- Ji, C., Hayes, G., 2008. Finite fault model: preliminary result of the May 12, 2008  $M_w$  7.9 eastern Sichuan, China earthquake. [http://earthquake.usgs.gov/earthquakes/eqinthenews/2008/us2008ryan/finite\\_fault.php](http://earthquake.usgs.gov/earthquakes/eqinthenews/2008/us2008ryan/finite_fault.php).
- Jia, S.X., Zhang, X.K., Zhao, J.R., et al., 2010a. Deep seismic sounding data reveal the crustal structures beneath Zoige basin and its surrounding folded orogenic belts. *Sci. China Ser. D-Earth Sci.* 53 (2), 203–212.
- Jia, D., Li, Y., Lin, A., et al., 2010b. Structural model of 2008  $M_w$  7.9 Wenchuan earthquake in the rejuvenated Longmen Shan thrust belt, China. *Tectonophysics* 491, 174–184.
- Jones, L.M., Han, W.B., Hauksson, E., et al., 1984. Focal mechanisms and aftershock locations of the Songpan earthquake of August 1976 in Sichuan, China. *J. Geophys. Res.* 89, 7697–7707.
- Kirby, E., Whipple, K.X., Burchfiel, B.C., Tang, W., Berger, G., Sun, Z., Chen, Z., 2000. Neotectonics of the Min Shan, China: implications for mechanisms driving Quaternary deformation along the eastern margin of the Tibetan plateau. *GSA Bull.* 112 (3), 375–393.
- Lei, J.S., Zhao, D.P., 2009. Structural heterogeneity of the Longmenshan fault zone and the mechanism of the 2008 Wenchuan earthquake ( $M_s$  8.0). *Geochem. Geophys. Geosyst.* 10 (10).
- Li, J.L., Yan, Z., Yu, L.J., Mu, P., 2007. Sedimentary and structural characteristics of the Rouergai–Songpan foreland basin. *Acta Petrol. Sin.* 23 (5), 919–924.
- Li, H., Su, W., Wang, C., et al., 2009a. Ambient noise Rayleigh wave tomography in western Sichuan and eastern Tibet. *Earth Planet. Sci. Lett.* 282, 201–211.
- Li, S., Mooney, W.D., Fan, J., 2006. Crustal structure of mainland China from deep seismic sounding data. *Tectonophysics* 420, 239–252.
- Li, S., Unsworth, M.J., Booker, J.R., Wei, W., Tan, H., Jones, A.G., 2003. Partial melt or aqueous fluid in the mid-crust of Southern Tibet? Constraints from INDEPTH magnetotelluric data. *Geophys. J. Int.* 153 (2), 289–304.
- Li, Y., Yao, H.J., Liu, Q.Y., 2010. Phase velocity array tomography of Rayleigh waves in western Sichuan from ambient seismic noise. *Chin. J. Geophys.* 53 (4), 842–852 (in Chinese).
- Li, Z.W., Roecker, S., Li, Z.H., et al., 2009b. Tomographic image of the crust and upper mantle beneath the western Tien Shan from the MANAS broadband deployment: possible evidence for lithospheric delamination. *Tectonophysics* 477, 49–57.
- Li, Z.W., Xu, Y., Huang, R., et al., 2011a. Crustal  $P$ -wave velocity structure of the Longmen Shan region and its tectonic implications for the 2008 Wenchuan earthquake. *Sci. China Earth Sci.* 54, 1386–1393.
- Li, Z.W., Hao, T.Y., Xu, Y., 2011b. Uppermost mantle structure of the North China Craton: constraints from interstation  $Pn$  traveltime difference tomography. *Chin. Sci. Bull.* 56, 1691–1699.
- Li, Z.W., Ni, S.D., Hao, T.Y., Xu, Y., Roecker, S., 2012. Uppermost mantle structure of the eastern margin of the Tibetan plateau from interstation  $Pn$  traveltime difference tomography. *Earth Planet. Sci. Lett.* 335–336, 195–205.
- Li, Z.W., You, Q.Y., Ni, S.D., Hao, T.Y., Wang, H.T., Zhuang, C.T., 2013a. Waveform retrieval and phase identification for seismic data from the CASS experiment. *Pure Appl. Geophys.* 170, 815–830.
- Li, Z.W., Tian, B.F., Liu, S., Yang, J.S., 2013b. Asperity of the 2013 Lushan earthquake in the eastern margin of Tibetan plateau from seismic tomography and aftershock relocation. *Geophys. J. Int.* 195, 2016–2022.
- Lin, G., Thurber, C.H., Zhang, H., Hauksson, E., Shearer, P.M., Waldhauser, F., Brocher, T.M., Hardebeck, J., 2010. A California statewide three-dimensional seismic velocity model from both absolute and differential times. *Bull. Seismol. Soc. Am.* 100, 225–240.
- Liu, Q.Y., Li, Y., Chen, J.H., et al., 2009. Wenchuan  $M_s$  8.0 earthquake: preliminary study of the  $S$ -wave velocity structure of the crust and upper mantle. *Chin. J. Geophys.* 52 (2), 309–319 (in Chinese).
- Lou, H., Wang, C.Y., Lv, Z.Y., et al., 2008. Deep tectonic setting of the 2008 Wenchuan  $M_s$  8.0 earthquake in southwestern China – Joint analysis of teleseismic  $P$ -wave receiver functions and Bouguer gravity anomalies. *Sci. China Ser. D-Earth Sci.* 52, 166–179.
- Luo, Y., Ni, S.D., Zeng, X.F., et al., 2010. A shallow aftershock sequence in the north-eastern end of the Wenchuan earthquake aftershock zone. *Sci. China Earth Sci.* 53, 1655–1664.
- McNamara, D.E., Walter, W.R., Owens, T.J., et al., 1997. Upper mantle velocity structure beneath the Tibetan plateau from  $Pn$  traveltime tomography. *J. Geophys. Res.* 102 (B1), 493–505.
- Molnar, P., Tapponnier, P., 1975. Cenozoic tectonics of Asia: effects of a continental collision. *Science* 189, 419–426.
- Molnar, P., 1988. A review of geophysical constraints on the deep structure of the Tibetan plateau, the Himalaya and the karakoram, and their tectonic implications. *Trans. R. Soc. Lond. Ser. A* 327, 33–88.
- Nelson, K.D., Zhao, W., Brown, L.D., et al., 1996. Partially molten middle crust beneath southern Tibet: synthesis of project INDEPTH results. *Science* 274 (5293), 1684–1688.
- Paige, C.C., Saunders, M.A., 1982. LSQR: an algorithm for sparse linear equations and sparse least squares. *TOMS* 8 (1), 43–71.
- Pei, S., Su, J., Zhang, H., Sun, Y., Toksöz, M.N., Wang, Z., Gao, X., Liu-Zeng, J., He, J., 2010. Three-dimensional seismic velocity structure across the 2008 Wenchuan  $M_s$  8.0 earthquake, Sichuan, China. *Tectonophysics* 491 (1), 211–217.
- Phillips, W.S., Rowe, C.A., Steck, L.K., 2005. The use of interstation  $P$  wave arrival time differences to account for regional path variability. *Geophys. Res. Lett.* 32, L11301.
- Phillips, W.S., Begnaud, M.L., Rowe, C.A., et al., 2007. Accounting for lateral variations of the upper mantle gradient in  $Pn$  tomography studies. *Geophys. Res. Lett.* 34, L14312.
- Rosenberg, C.L., Handy, M.R., 2005. Experimental deformation of partially melted granite revisited: implication for the continental crust. *J. Metamorph. Geol.* 555, 1–9.
- Royden, L.H., Burchfiel, B.C., King, R.W., et al., 1997. Surface deformation and lower crustal flow in eastern Tibet. *Science* 276, 788–790.
- Royden, L.H., Burchfiel, B.C., van der Hilst, R.D., 2008. The geological evolution of the Tibetan plateau. *Science* 321, 1054–1058.
- Seward, A.M., Henderson, C.M., Smith, E.G.C., 2009. Models of the upper mantle beneath the central North Island, New Zealand, from speeds and anisotropy of subhorizontal  $P$  waves ( $Pn$ ). *J. Geophys. Res.* 114, B01301.
- Shen, Z.K., Sun, J.B., Zhang, P.Z., et al., 2009. Slip maxima at fault junctions and rupturing of barriers during the 2008 Wenchuan earthquake. *Nat. Geosci.* 2, 718–724.
- Steck, L.K., Phillips, W.S., Mackey, K., Begnaud, M.L., Stead, R.J., Rowe, C.A., 2009. Seismic tomography of crustal  $P$  and  $S$  across Eurasia. *Geophys. J. Int.* 177, 81–92.

- Steck, L.K., Begnaud, M.L., Phillips, S., Stead, R., 2011. Tomography of crustal  $P$  and  $S$  travel times across the western United States. *J. Geophys. Res.* 116, B11304.
- Waldhauser, F., Ellsworth, W.L., 2000. A double-difference earthquake location algorithm: method and application to the northern Hayward Fault, California. *Bull. Seismol. Soc. Am.* 90, 1353–1368.
- Wang, W.M., Zhao, L.F., Li, J., et al., 2008. Rupture process of the  $M_s$  8.0 Wenchuan earthquake of Sichuan. *Chin. J. Geophys.* 51 (5), 1403–1410.
- Wang, X.B., Zhu, Y.T., Zhao, X.K., et al., 2009. Deep conductivity characteristics of the Longmen Shan, Eastern Qinghai-Tibet plateau. *Chin. J. Geophys.* 52 (2), 564–571.
- Wang, C.Y., Lou, H., Silver, P.G., et al., 2010. Crustal structure variation along 30°N in the eastern Tibetan plateau and its tectonic implications. *Earth Planet. Sci. Lett.* 289, 367–376.
- Wei, W., Zhao, D., Xu, J.D., 2013.  $P$ -wave anisotropic tomography in southeast Tibet: new insight into the lower crustal flow and seismotectonics. *Phys. Earth Planet. Inter.* 222, 47–57.
- Wu, J.P., Huang, Y., Zhang, T.Z., et al., 2009. Aftershock distribution of the  $M_s$  8.0 Wenchuan earthquake and three dimensional  $P$ -wave velocity structure in and around source region (in Chinese). *Chin. J. Geophys.* 52 (2), 320–328.
- Xu, Y., Li, Z., Huang, R., et al., 2010. Seismic structure of the Longmen Shan region from  $S$ -wave tomography and its relationship with the Wenchuan  $M_s$  8.0 earthquake on 12 May 2008, Southwestern China. *Geophys. Res. Lett.* 37, L02304.
- Yao, H., Beghein, C., van der Hilst, R.D., 2008. Surface-wave array tomography in SE Tibet from ambient seismic noise and two-station analysis: II-Crustal and upper mantle structure. *Geophys. J. Int.* 173, 205–219.
- Yang, Y., Zheng, Y., Chen, J., et al., 2010. Rayleigh wave phase velocity maps of Tibet and the surrounding regions from ambient seismic noise tomography. *Geochem. Geophys. Geosyst.* 11, Q08010.
- Yin, H.F., Wu, S.B., Du, Y.S., et al., 1999. South China defined as part of Tethyan archipelagic ocean system. *Earth Sci. J. China Univ. Geosci.* 24 (1), 1–12.
- Yin, A., Harrison, T.M., 2000. Geologic evolution of the Himalayan-Tibetan orogen. *Annu. Rev. Earth Planet. Sci.* 28 (1), 211–280.
- Zhan, Y., Zhao, G.Z., Unsworth, M., et al., 2013. Deep structure beneath the southwestern section of the Longmenshan fault zone and seismogenetic context of the 4.20 Lushan  $M_s$  7.0 earthquake. *Chin. Sci. Bull.* 58. <http://dx.doi.org/10.1007/s11434-013-6013-x>.
- Zhao, G.Z., Chen, X.B., Xiao, Q.B., et al., 2009. Generation mechanism of Wenchuan strong earthquake of  $M_s$  8.0 inferred from EM measurements in three levels. *Chinese J. Geophys.* 52 (2), 553–563.
- Zhang, H., Thurber, C.H., 2003. Double-difference tomography: the method and its application to Hayward Fault, California. *Bull. Seismol. Soc. Am.* 93, 1875–1889.
- Zhang, P.Z., Xu, X.W., Wen, X.Z., et al., 2008. Slip rates and recurrence intervals of the Longmen Shan active fault zone, and tectonic implications for the mechanism of the May 12 Wenchuan earthquake, 2008, Sichuan, China (in Chinese). *Chin. J. Geophys.* 51 (4), 1066–1073.
- Zhang, Z., Wang, Y., Chen, Y., et al., 2009. Crustal structure across Longmenshan fault belt from passive source seismic profiling. *Geophys. Res. Lett.* 36, L17310.
- Zhang, Z.J., Yuan, X.H., Chen, Y., et al., 2010. Seismic signature of the collision between the east Tibetan escape flow and the Sichuan basin. *Earth Planet. Sci. Lett.* 2010 (292), 254–264.
- Zheng, Y., Ma, H., Lu, Y., et al., 2009. Source mechanism of strong aftershocks ( $M_s \geq 5.6$ ) of the 2008/05/12 Wenchuan earthquake and the implication for seismotectonics. *Sci. China Ser. D-Earth Sci.* 52, 739–753.
- Zheng, Y., Ni, S.D., Xie, Z.J., Lv, J., Ma, H., Sommerville, P., 2010. Strong aftershocks in the northern segment of the Wenchuan earthquake rupture zone and their seismotectonic implications. *Earth Planet Space* 62 (11), 881–886.
- Zheng, Y., Ge, C., Xie, Z.J., Yang, Y.J., Xiong, X., Hsu, H., 2013. Crustal and upper mantle structure and the deep seismogenic environment in the source regions of the Lushan earthquake and the Wenchuan earthquake. *Sci. China Earth Sci.* 56 (7), 1158–1168.